PHYSICAL REVIEW B **105**, 115115 (2022)

Ab initio calculation of the effective Coulomb interactions in MX_2 (M=Ti, V, Cr, Mn, Fe, Co, Ni; X=S, Se, Te): Intrinsic magnetic ordering and Mott phase

A. Karbalaee Aghaee,[1] S. Belbasi,[1] and H. Hadipour[2,*]
[1]*Department of Physics, Faculty of Science, University of Zanjan, 45371-38791, Zanjan, Iran*
[2]*Department of Physics, University of Guilan, 41335-1914, Rasht, Iran*

(Received 15 January 2022; revised 15 February 2022; accepted 15 February 2022; published 10 March 2022)

Correlated phenomena such as magnetism and the Mott phase are a very controversial issues in two-dimensional transition metal dichalcogenides (TMDCs). Intending to find the value of the correlation strength and understanding the origin of ferromagnetic order in TMDCs, we first identify relevant, low-energy degrees of freedom on both octahedral $1T$ and trigonal prismatic $2H$ structures in $3d$-MX_2 (M = Ti, V, Cr, Mn, Fe, Co, Ni; X = S, Se, Te) and then determine the strength of the effective Coulomb interactions between localized d electrons from the first principles using the constrained random-phase approximation. The on-site Coulomb interaction values lie in the range 1.4–3.7 eV (1.1–3.6 eV) for the $1T$ structure ($2H$ structure) and depend on the ground-state electronic structure, d-electron number, and correlated subspace. For most of the $3d$-TMDCs, we obtain $1 < U/W_b < 2$ (the bandwidth W_b), which turn out to be larger than the corresponding values in elementary transition metals. Based on the calculated U and exchange J interaction, we check the condition to be fulfilled for the formation of the ferromagnetic order by the Stoner criterion. The results indicate that experimentally observed MnX_2 (X = S, Se) and VX_2 (X = S, Se) have an intrinsic ferromagnetic behavior in pristine form, although V-based materials are close in vicinity to the critical point separating the ferromagnetic from the paramagnetic phase.

DOI: 10.1103/PhysRevB.105.115115

I. INTRODUCTION

Electron correlation has been an important issue in low-dimensional systems after the experimental synthesis of graphene [1,2] and other two-dimensional (2D) materials [3–5]. Generally, 2D compounds have less bandwidth than the bulk due to larger discreteness of the density of states (DOS) and lower number of screening channels, as a consequence, the strength of the correlation U/W_b, namely the ratio of the effective electron-electron interaction U to bandwidth W_b, becomes great [6]. For 2D materials containing transition metal (TM) atoms, in addition to quantum confinement effects arising from reduced dimensionality, due to the presence of narrow t_{2g} or e_g states at the vicinity of Fermi level (E_F), correlation effects are even stronger and play a crucial role in determining the electronic and magnetic properties [7]. One of the consequences of a moderate correlation $U/W_b \sim 1$ or strong correlation $U/W_b \gg 1$ are inducing magnetic ordering [7,8], Mott insulator [7,9–11], and so on in low-dimensional systems. For instance, an intrinsic ferromagnetism in the monolayers of TM halides such as CrX_3 (X=Cl, Br, I) [12–17], VI$_3$ [18,19], NiI$_2$ [20] has been observed experimentally and confirmed theoretically [21–25]. Furthermore, due to the large correlation strength $U/W_b > 2$, most of the TM halides exhibit a Mott insulating character especially in the systems with nearly half-filled $3d$ bands [7]. Besides TM halides, other 2D materials such as in Cr$_2$Ge$_2$Te$_6$ [4], Fe$_3$GeTe$_2$ [26,27], VX_2 (X=Se,Te) [28–33], TiTe$_2$ [34], MnSe$_2$ [35], CrX_2 (X=S, Se, Te) [36–42], $1T$-TaX_2 [43,44], and TM phosphorous trichalcogenides [45] like NiPX_3, have been experimentally found to show magnetic orderings or Mott phase.

In the mentioned systems, synthesis of the $3d$ TM dichalcogenides (TMDCs) such as MX_2 (M=V, Cr, Mn; X=S, Se, Te) has led to a huge experimental and theoretical interest due to the existence of incredibly rich correlated phenomena ranging from room-temperature intrinsic ferromagnetism [5,30–35] to charge density wave order [46–48], and the Mott phase [10,11]. Experimentally, even at room temperature, ferromagnetic order was reported in Mn- and V-based MX_2 compounds [30,35]. The possibility of 100% spin polarization indicates that MX_2 monolayers are a promising material for spintronics devices. Also, including the on-site Coulomb interaction leads to Mott insulating behavior for V-based systems due to the presence of a half-filled band [10]. However, for most of the $3d$-TMDCs such as CrX_2, MnX_2 systems, and even VX_2, the origin of the intrinsic ferromagnetism remains controversial and the existence of a strongly correlated phase is still in doubt [29,48–52]. In other words, some other opposite studies indicated that the ferromagnetism seen in the $3d$-TMDCs is extrinsic 2D magnetism stemming from vacancies [53] or proximity effects [52,54], which are not able to be precisely eliminated in 2D crystal growth. The formation of such extrinsic magnetic moments and long-range magnetic order induced by atom vacancies in some other 2D nonmagnetic materials such as graphene [55–58] and MoS$_2$ [59,60] makes the absence of intrinsic 2D

---

[*] hanifhadipour@gmail.com

magnetism for pristine TMDCs more likely. From the theoretical side, magnetic ordering depends strongly on the correlated subspace of the d-shell and its value of the electron correlation [51]. Anyway, controversy exists over the intrinsic magnetism in the monolayer of 3d-TMDCs. Another interesting property of 3d-TMDCs such as trigonal prismatic single layer of CrX_2 and VX_2 is valley polarization [11,61]. Most of the valleytronic MX_2 have an appropriate spin-polarized band gap of 1.0 eV and spontaneous valley polarization are found to be about 40–90 meV [61,62], large enough for valleytronic devices. The presence of both large valley polarization and spin splitting in a single material is attractive for the research on valleytronic and spintronic applications.

On the computational side, to prevail over the problems of band-gap underestimation in density functional theory (DFT) based on the local density approximation (LDA) or generalized gradient approximation (GGA) and to improve band dispersion to find proper valley polarization, GWA (in particular self-consistent GW +spin orbit coupling) was performed to induce many-body correction [49,63–66]. However, due to the presence of narrow d bands in TMDCs monolayer, the methods that allow for the treatment of strong local correlations such as DFT + U and DFT plus dynamical mean-field theory (DFT + DMFT) will be needed. The DFT + U method was employed to study the electronic properties of some 3d-TMDCs [36,67,68] in which the effective U parameters are usually taken from the values found for other materials including the same transition metal atom. Indeed, the results of this approach are not extensive and usually are not consistent with those extracted from experiments. Only a few works have been performed by *ab initio* linear response theory and constraint random phase approximation (cRPA) [69–71] to calculate the Hubbard U for VS$_2$ [10,72]. This motivates us to do a fully *ab initio* calculation to find the effective Coulomb parameters for all 3d-TMDC monolayers. The U parameters obtained from *ab initio* calculations not only provide a fundamental understanding of the correlated phenomena in TMDCs, but also these effective interactions can also be used in model Hamiltonians, thus increasing the predictive power of model calculations.

In this systematic study, we first identify appropriate correlated subspaces by constructing the Wannier function and then by employing the cRPA approach within the full-potential linearized augmented-plane-wave (FLAPW) method. We determine the effective on-site Coulomb interaction of the d electrons in MX_2 (M=Ti, V, Cr, Mn, Fe, Co, Ni; X=S, Se, Te) for both 2H and 1T structures. We find $1 < U/W_b < 2$ in most 3d-MX_2, making them moderately correlated materials. In the nonmagnetic state, among the metallic 3d-TMDCs, the maximum correlation strength U/W_b turns out to be 2.7 in 1T-MnS_2 and 1.5 in 2H-VS_2 with values much larger than the corresponding values in elementary TMs. Based on U and the exchange interaction J values, we discuss the tendency of the electron spins to order ferromagnetically by Stoner criterion. The results indicate that experimentally observed MnX_2 (X=S, Se) and VX_2 (X=S, Se) have an intrinsic ferromagnetic behavior in pristine forms. Moreover, V-based materials are close to the edge of paramagnetic to ferromagnetic transition

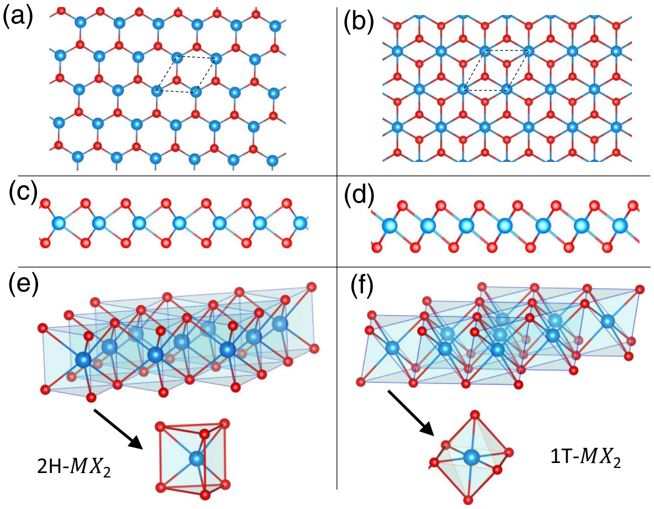

FIG. 1. Top view of the two-dimensional crystal of MX_2 for (a) 2H single layer, (b) 1T single layer. Side view of MX_2 for (c) 2H and (d) 1T structures. (e) Trigonal prismatic coordination of one TM and six chalcogen X atoms in 2H structure. (f) Octahedral coordination in 1T structure where in each TM atoms are bound to six X atoms. The blue and red spheres exhibit M and X atoms, respectively.

II. COMPUTATIONAL DETAILS

A. Crystal structure and correlated subspace

There are two common types of crystal structures in the monolayer of TMDCs, which are trigonal prismatic (2H) and octahedral (1T) coordination [73]. The side and top views of the crystal structures of 1T and 2H single layer of MX_2 systems are presented in Figs. 1(a) to 1(d). The difference in crystal field splitting generated by surrounding chalcogen X atoms for two lattices of 2H-MX_2 and 1T-MX_2 leads to different correlated subspace and plays a key role in expressing the differences in the observed electronic and magnetic properties. So, we first briefly describe the crystal structural of MX_2 in 1T and 2H lattices. A single layer of 1T-MX_2 consists of triangular nets of TM atoms so that the X atoms are arranged as octahedra with M atoms in the center [see Fig. 1(f)]. In this arrangement, d electrons states splits into three lower-energy orbitals t_{2g} (d_{xy}, d_{xz}, d_{yz}) and two higher-energy orbitals e_g (d_{z^2}, $d_{x^2-y^2}$). Note that the octahedron is tilted with respect to the standard Cartesian coordinate x, y, z system, in such a way that C_4 axes (the axes goes through two opposite vertices of the octahedron) is in the z' direction and the two opposite faces of the octahedron are parallel to the layers [74,75]. As shown in Figs. 2(a) and 2(b), in fact, one of the eight triangles of the octahedron is lying on the floor and the z axis is perpendicular to this triangle. In this situation, the linear combination of the local t'_{2g} orbitals, namely $d_{x'y'}$, $d_{x'z'}$, $d_{y'z'}$ will be the low-energy levels. Using the rotation matrix

$$\begin{pmatrix} 2/\sqrt{6} & -1/\sqrt{6} & 1/\sqrt{6} \\ 0 & 1/\sqrt{2} & -1/\sqrt{2} \\ 1/\sqrt{3} & 1/\sqrt{3} & 1/\sqrt{3} \end{pmatrix}, \tag{1}$$

the singlet d_{z^2} orbital which is oriented perpendicular to the layer, is given by $(d_{x'y'} + d_{x'z'} + d_{y'z'})/\sqrt{3}$. The other t'_{2g}

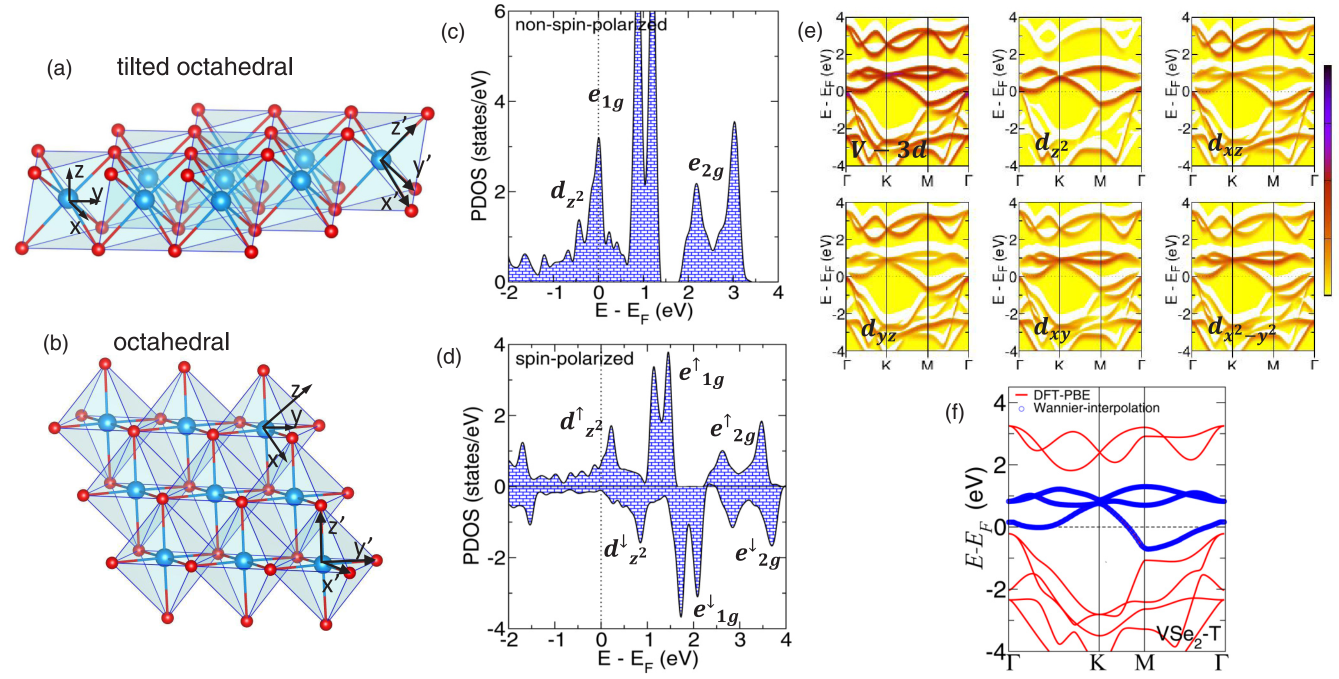

FIG. 2. (a) Tilted octahedral crystal structure with respect to the standard x, y, z Cartesian coordinate in $1T$ single layer where in two opposite faces of the octahedron are parallel to the layers. (b) The same structure in the rotated state x', y', z' so that it forms a conventional octahedral phase. (c) DOS projected onto $3d$ states of the V atom in the non-spin-polarized calculation for $1T$-VSe$_2$. (d) The same as (c) for spin-polarized calculation. (e) The orbital-projected band structures for $3d$ electrons of V atom of $1T$-VSe$_2$ based on DFT-PBE. (f) DFT-PBE (red) and Wannier interpolated band structures (blue) of $1T$-VSe$_2$ monolayer using $d_{z^2} + e_{g1}$ subspace.

orbitals, $(d_{y'z'} - d_{x'y'})/\sqrt{2}$, and $(d_{y'z'} + d_{x'y'} - 2d_{x'z'})/\sqrt{6}$, correspond to the doublet e_{1g} states. The two $d_{z^2}/d_{x'^2-y'^2}$ are denoted by high-energy degenerate doublets e_{2g} states. By these notations, the non-spin polarized density of d states for $1T$-VSe$_2$ are presented in Fig. 2(c). Note that the bands are not of pure d_{z^2}, e_{1g}, and e_{2g} character but are mixtures. Thus, this nominations like d_{z^2} refer to their dominant orbital character.

For $2H$-MX_2, because of the trigonal prismatic coordination Fig. 1(e), in the crystal-field level, the d-shell splits into a singlet d_{z^2}, an intermediate energy doublet e_g (d_{xy} and $d_{x^2-y^2}$), and a high-energy doublet e'_g (d_{xz}, d_{yz}) states. According to this notation, in Fig. 3(a) we presented the non-spin-polarized density of d states for $2H$ monolayer of VSe$_2$.

The basic unit cell is hexagonal in all $3d$-TMDCs and consists of three atoms. We consider MX_2 (M=Ti, V, Cr, Mn, Fe, Co, Ni; X=S, Se, Te) for both $1T$ and $2H$ structures. MX_2 unit cells containing one M and two X atoms are simulated based on the slab model having a 25 Å vacuum separating them. For the non-spin-polarized as well as for the spin-polarized DFT calculations, the FLAPW method as implemented in the FLEUR code [76,77] is used.

We employ GGA in the Perdew-Burke-Ernzerhof (PBE) parametrization [78] for the exchange-correlation energy functional. Since Coulomb matrix elements are sensitive to the internal coordinates of the atoms and structural distortions, for all calculations the lattice parameters and atomic positions are chosen to be equal to the optimized parameters with considering the relaxation of the atomic coordinates and possible distortions. So, the coordinates of two X atoms are optimized with the residual force less than 0.01 eV/Å. In the scf calculation, $16 \times 16 \times 1$ k-point grids are used for unit cells of all systems. A linear momentum cutoff of $G_{\max} = 4.5$ bohr^{-1} is chosen for the plane waves. The maximally localized Wannier functions (MLWFs) are constructed with the WANNIER90 library [79] using appropriate bands per M atom. The DFT calculations are used as an input for the SPEX code [80,81] to determine the strength of the Coulomb interaction between correlated electrons from the cRPA and RPA methods [70,71]. A dense k-point grid $12 \times 12 \times 1$ is used in the calculation of dielectric function.

To find the strength of the screened Coulomb interaction we need to identify the correlated subspace which helps to construct Wannier functions properly. So, first, we calculate both nonmagnetic and magnetic orbital-resolved DOS for all systems which will be discussed in the next section in detail. Here, we only presented the orbital projected band structure of VSe$_2$ in two structures, namely $1T$-VSe$_2$ and $2H$-VSe$_2$, in Figs. 2(e) and 3(b), respectively, that resolve the contribution of different d states. The reason why we chose the VSe$_2$ case is that the origin of the ferromagnetism and Mott phase in its monolayer limit is still under debate. Also, it was one of the first materials in $3d$-TMDCs, in which ferromagnetism is detected experimentally in the monolayer limit.

As shown in Fig. 2(e) in the $1T$ structure, in the nonmagnetic calculation the mixture of d_{z^2} and e_{1g} ($d_{xy}/d_{x^2-y^2}$) is significant which is also observed in total DOS of d states [see Fig. 2(c)], in such way that t'_{2g} ($d_{z^2} + e_{1g}$) states are well-isolated bands at the vicinity of E_F. Although, we construct Wannier functions individually for single d_{z^2}, three t'_{2g},

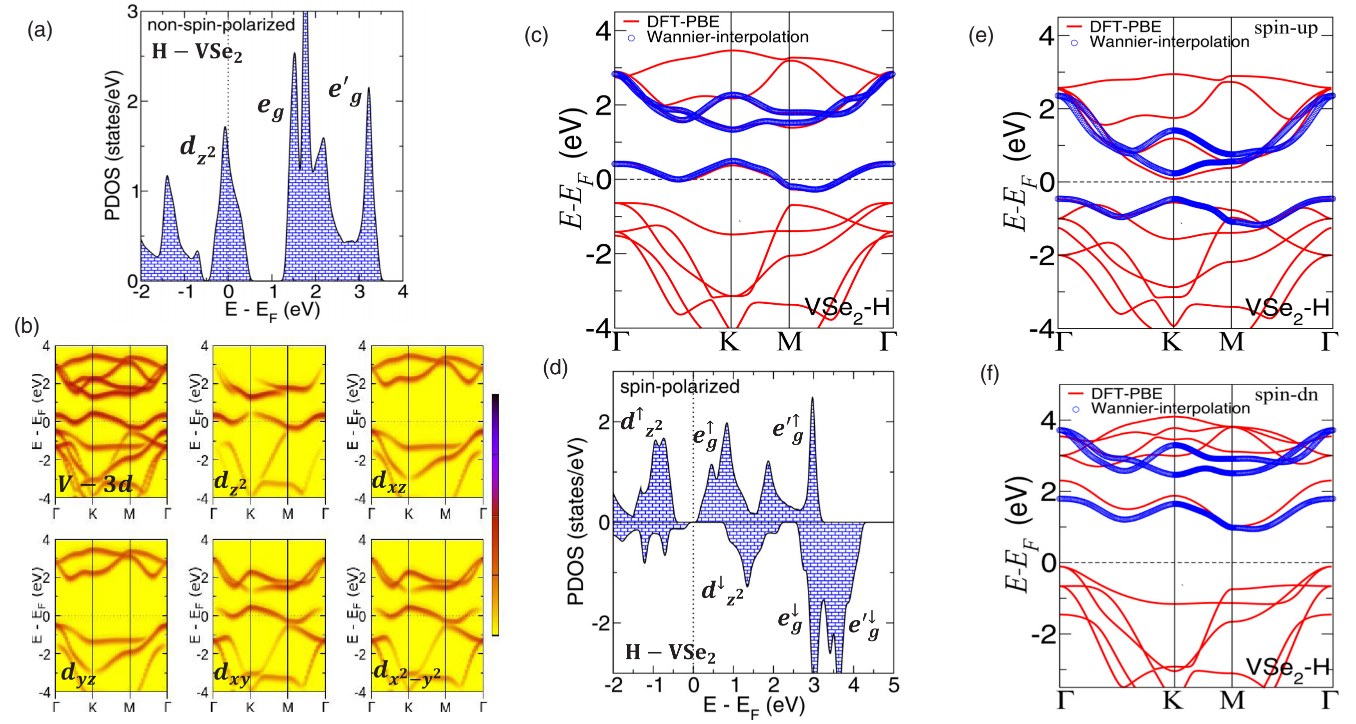

FIG. 3. (a) DOS projected onto $3d$ states of the V atom in the non-spin-polarized calculation for $2H$-VSe$_2$. (b) The orbital-projected band structures for $3d$ electrons of V atom of $2H$-VSe$_2$ based on DFT-PBE. (c) DFT-PBE (red) and Wannier interpolated band structures (blue) of $2H$-VSe$_2$ monolayer using $d_{z^2} + e_g$ subspace. (d) The same as (a) for spin-polarized calculation. DFT-PBE and Wannier interpolated band structures of $2H$-VSe$_2$ monolayer using $d_{z^2} + e_g$ subspace for (e) spin up and (f) spin down.

and the full d shell orbitals as a correlated subspace. In the t'_{2g} and d cases, the original and the Wannier-interpolated bands agree very well. In Fig. 2(f), we presented a comparison of the non-spin-polarized DFT-PBE band structures with the corresponding Wannier-interpolated bands obtained with the t'_{2g} Wannier orbitals as a minimal subspace for $1T$ structure of VSe$_2$. In other words, it motivates a three-band model for VSe$_2$ with t'_{2g} Wannier orbitals. In the same way, correlated subspaces are defined for all considered $1T$ structures of TMDCs, which will be discussed in the next section.

In the $2H$-VSe$_2$, a single half-filled band which is predominantly d_{z^2} orbital character is well separated from the other bands in the nonmagnetic calculation [see Fig. 3(a)]. Thus, to find the minimal correlated subspace in the $2H$ structures we construct Wannier functions for the d_{z^2}, e_g orbitals. These energy levels are mainly responsible for the electronic, magnetic, and transport properties of $2H$-VSe$_2$. Note that e'_g states are far from the E_F and do not contribute to constructing a half-filled band at E_F. The comparison of the DFT-PBE band structure with Wannier interpolation [see Fig. 3(c)] indicates that the best consistency can be obtained by $d_{z^2} + e_g$ Wannier orbitals as a minimal subspace.

Note that, since one of the aims of this paper is to determine effective Coulomb parameters for the low-energy model Hamiltonian of correlated TM materials, the results before symmetry breaking take place, such as nonmagnetic U, should be calculated. Despite this, we have done the spin-polarized calculations for a few systems. As shown in Figs. 2(d) and 3(d), the crystal field splitting is small in $3d$-TMDC materials compared to exchange splitting. So, considering spin polarization may cause to have problems with entangled bands. It complicates the construction of the Wannier function if we use $d_{z^2} + e_g$ subspace in the magnetic calculation. As shown in Figs. 3(e) and 3(f), the original and the Wannier-interpolated bands do not agree very well. In this case, we must go beyond the $d_{z^2} + e_g$ minimal subspace, for instance, the full d-shell subspace, which eliminates a few specific states in the screening.

Note that for a few materials, in particular, Te-based systems in the nonmagnetic calculation, we require a few more states in the construction of the Wannier due to the entanglement of d bands of M atoms with p bands of X atoms at some parts of the Brillouin zone. Several procedures have been proposed in the literature to calculate the polarization function for entangled bands [6,70,71]. In this work we use the method described in Ref. [6]. To confirm the reliability of crystal structure analysis we described and validity of Wannier functions, the d_{z^2}/e_{1g}-like MLWFs for $1T$-VSe$_2$, and d_{z^2}/e_g-like MLWFs for $2H$-VSe$_2$ are presented in Figs. 4(a) and 4(b).

B. cRPA method and construction of the matrix elements

In the following, we briefly describe the cRPA method. The fully screened Coulomb interaction $\tilde{U}$ is related to the bare Coulomb interaction V by

$$\tilde{U}(\mathbf{r},\mathbf{r}',\omega) = \int d\mathbf{r}'' \epsilon^{-1}(\mathbf{r},\mathbf{r}'',\omega) V(\mathbf{r}'',\mathbf{r}'), \qquad (2)$$

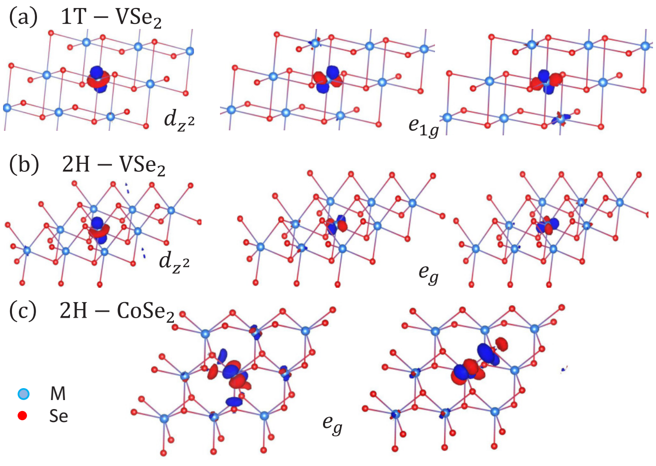

FIG. 4. (a) The d_{z^2}- and e_{1g}-like MLWF for V atom of $1T$-VSe$_2$. (b) The d_{z^2}- and e_g-like MLWF for V atom of $2H$-VSe$_2$. (c) The e_g-like MLWF for Co atom of $2H$-CoSe$_2$.

where $\epsilon(\boldsymbol{r},\boldsymbol{r}'',\omega)$ is the dielectric function. The dielectric function is related to the electron polarizability P by

$$\epsilon(\boldsymbol{r},\boldsymbol{r}',\omega)=\delta(\boldsymbol{r}-\boldsymbol{r}')-\int d\boldsymbol{r}''V(\boldsymbol{r},\boldsymbol{r}'')P(\boldsymbol{r}'',\boldsymbol{r}',\omega), \tag{3}$$

where the RPA polarization function $P(\boldsymbol{r}'',\boldsymbol{r}',\omega)$ is given by

$$P(\boldsymbol{r},\boldsymbol{r}',\omega)=2\sum_{m}^{\text{occ}}\sum_{m'}^{\text{unocc}}\varphi_m(\boldsymbol{r})\varphi^*_{m'}(\boldsymbol{r})\varphi^*_m(\boldsymbol{r}')\varphi_{m'}(\boldsymbol{r}')\times\left[\frac{1}{\omega-\Delta_{mm'}+i\eta}-\frac{1}{\omega+\Delta_{mm'}-i\eta}\right]. \tag{4}$$

Here, $\varphi_m(\boldsymbol{r})$ are the single-particle DFT Kohn-Sham eigenfunctions, and η a positive infinitesimal. $\Delta_{mm'}=\epsilon_{m'}-\epsilon_m$ with the Kohn-Sham eigenvalues ϵ_m.

In the cRPA approach, to exclude the screening due to the correlated subspace, we separate the full polarization function of Eq. (4) into two parts

$$P=P_d+P_r, \tag{5}$$

where P_d includes only the transitions ($m\rightarrow m'$) between the states of the correlated subspace and P_r is the remainder. Then, the frequency-dependent effective Coulomb interaction is given schematically by the matrix equation

$$U(\omega)=[1-VP_r(\omega)]^{-1}V. \tag{6}$$

It contains, in P_r, screening processes that would not be captured by the correlated subspace and excludes the ones that take place within the subspace.

The matrix elements of the effective Coulomb interaction in the MLWF basis are given by

$$U_{\mathbf{R}n_1,n_3,n_2,n_4}(\omega)=\iint d\boldsymbol{r}d\boldsymbol{r}'w^*_{n_1\mathbf{R}}(\boldsymbol{r})w_{n_3\mathbf{R}}(\boldsymbol{r})\times U(\boldsymbol{r},\boldsymbol{r}',\omega)w^*_{n_4\mathbf{R}}(\boldsymbol{r}')w_{n_2\mathbf{R}}(\boldsymbol{r}'), \tag{7}$$

where $w_{n\mathbf{R}}(\boldsymbol{r})$ is the MLWF at site $\mathbf{R}$ with orbital index n, and the effective Coulomb potential $U(\boldsymbol{r},\boldsymbol{r}',\omega)$ is calculated within the cRPA as described above. We define the average Coulomb matrix elements U, U', and J in the static limit ($\omega=0$) as follows [82,83]:

$$U=\frac{1}{L}\sum_m U_{mm;mm}, \tag{8}$$

$$U'=\frac{1}{L(L-1)}\sum_{m\neq n}U_{mn;mn}, \tag{9}$$

$$J=\frac{1}{L(L-1)}\sum_{m\neq n}U_{mn;nm}, \tag{10}$$

where L is the number of localized orbitals, i.e., two for e_g and three for t_{2g} orbitals. This parametrization of partially screened Coulomb interactions is the so-called Hubbard-Kanamori parametrization. Similar to the definition of U (U', J), we can also define the so-called fully screened interaction parameters $\tilde{U}$ ($\tilde{U'}$, $\tilde{J}$) as well as unscreened (bare) V. The bare V provides information about the localization of Wannier functions and is a useful parameter in the interpretation of the screened Coulomb interaction parameters.

III. RESULTS AND DISCUSSION

A. Finding of correlated subspace

We start with the discussion of appropriate correlated subspace moving from early TiX_2 to late NiX_2 for both $1T$ and $2H$ structures. To define correlated subspace and also to identify the contribution of different M atoms in the screening, in Fig. 5 we present a nonmagnetic orbital-resolved DOSs for all considered MX_2 in $1T$ structure. Similar to the V-based system, the comparison of the DFT-PBE band structure with Wannier interpolation shows that for all compounds except Ni-based $1T$-MX_2, the bands with t'_{2g} ($d_{z^2}+e_{1g}$) character is the well-defined correlated subspace. This result is to be expected because of the existence of large density of t'_{2g} states near the E_F for TiX_2 to CoX_2. In the case of $1T$-NiX_2 systems (see the last column of Fig. 5), the Fermi levels are located in the energy gap between t'_{2g} and e_{2g} bands and the minimal correlated subspace depends on the type of electron or hole doping. The original and the Wannier-interpolated bands do not agree very well when we consider subspace t'_{2g}. For these systems, we defined e_{2g}, and full d states as correlated subspace. It means e_{2g} is a well-defined subspace in zero-doping, but for optical properties and other correlated phenomena the d subspace would be necessary. As shown in Fig. 5, the orbital-resolved DOS of $1T$-MX_2 with $X=$ S, Se, Te look very similar, thus we determined Hubbard U parameters identically moving from X=S to Te systems. Figure 5 exhibits a strong admixture of chalcogen p with t'_{2g} states which increase as one moves from M=Ti to Ni-based systems and also from X=S to Te ones. To find correlated subspace in these cases, we included a few more states in the construction of the Wannier functions. We find U matrix elements of, for example, p-admixed t'_{2g} states and pure t'_{2g} are nearly identical. However, the delocalization effect arising from the admixture of p states will be reflected in the value of Coulomb parameters later.

For the $2H$ structure of MX_2, the situation for defining the proper subspace is more complicated and differs from one

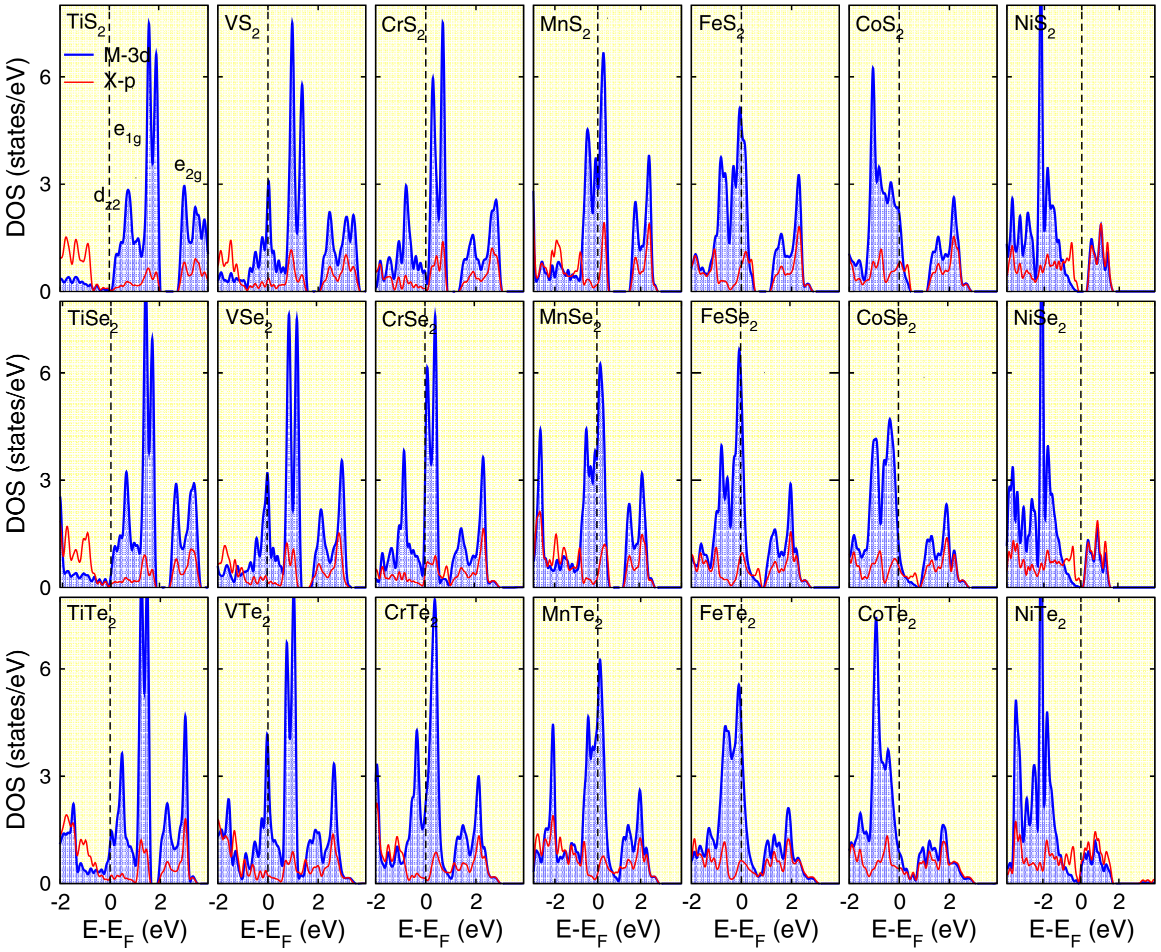

FIG. 5. DOS projected onto $3d$ states of the M atom as well as on p states of the X atoms for $1T$-MX_2 materials. The three distinct peaks of d bands correspond to d_{z^2}, e_{1g}, and e_{2g} states.

system to another one. The behavior of the electronic structure of $3d$ orbitals across the TM atoms, from X=S to Te, is similar to the case of $1T$ structure. So, we only depicted the orbital resolved DOS only for MSe$_2$ materials in Fig. 6. For Ti- and V-based MX_2, although a single band with predominantly d_{z^2} character is well separated from the other states, but the best consistency is given by $d_{z^2} + e_g$ states. However, because of the great importance of the single d_{z^2} band which almost allows defining an effective single band low-energy Hamiltonian, we also reported the electron-electron interactions for this single band correlated subspace. In CrX_2 to FeX_2, we see the substantially contribution of both d_{z^2} and e_g states to the DOS around e_F, as a consequence, bands with predominantly $d_{z^2} + e_g$ character are obtained to construct the Wannier function properly. For the last two series, namely $2H$-CoX_2 and $2H$-NiX_2, we find e_g and e'_g, respectively, as the minimal correlated subspaces and these layers can be described by a two-orbital effective low-energy model. Although a four-orbital $e_g + e'_g$ low-energy model can be used for the Ni case with caution.

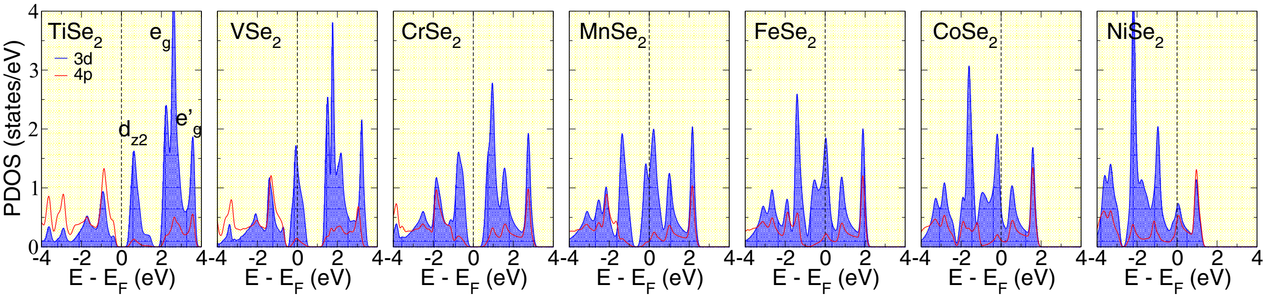

FIG. 6. DOS projected onto $3d$ states of the M atom as well as on p states of the Se atoms for $2H$-MSe$_2$ materials. The three distinct peaks of d bands correspond to d_{z^2}, e_g, and e'_g states.

TABLE I. Lattice parameter, orbital type of correlated subspace, bandwidth W_b, on-site intraorbital bare V, intraorbital partially (fully) screened $U(\tilde{U})$, interorbital partially (fully) screened $U'(\tilde{U}')$, partially (fully) screened exchange interaction $J(\tilde{J})$, correlation strength U/W_b, and the DOS at the Fermi level $D(E_F)$ for $1T$-MX_2 compounds.

MX_2	a (Å)	Orbitals	W_b (eV)	V (eV)	$U(\tilde{U})$ (eV)	$U'(\tilde{U}')$ (eV)	$J(\tilde{J})$ (eV)	U/W_b	$D(E_F)$
TiS_2	3.4176	$d_{z^2}+e_{1g}$	1.85	15.12	2.22(1.56)	1.41(0.98)	0.40(0.29)	1.20	0.07
$TiSe_2$	3.5441	$d_{z^2}+e_{1g}$	1.81	14.69	1.85(1.27)	1.04(0.67)	0.40(0.29)	1.02	0.38
$TiTe_2$	3.7409	$d_{z^2}+e_{1g}$	1.98	13.08	1.36(0.96)	0.68(0.49)	0.33(0.22)	0.69	1.15
VS_2	3.1917	$d_{z^2}+e_{1g}$	2.17	16.25	2.56(0.93)	1.69(0.48)	0.43(0.22)	1.18	3.12
VSe_2	3.3341	$d_{z^2}+e_{1g}$	1.92	16.09	2.14(0.83)	1.29(0.40)	0.42(0.21)	1.11	3.26
VTe_2	3.6020	$d_{z^2}+e_{1g}$	2.34	14.47	1.77(0.63)	1.02(0.29)	0.36(0.16)	0.76	4.31
CrS_2	3.0656	$d_{z^2}+e_{1g}$	2.07	16.68	2.78(1.12)	1.93(0.16)	0.42(0.21)	1.35	0.30
$CrSe_2$	3.2243	$d_{z^2}+e_{1g}$	2.16	16.14	2.49(0.60)	1.75(0.12)	0.38(0.17)	1.16	5.80
$CrTe_2$	3.6932	$d_{z^2}+e_{1g}$	2.12	15.59	2.27(0.48)	1.52(0.30)	0.37(0.14)	1.07	4.23
MnS_2	3.3507	$d_{z^2}+e_{1g}$	1.12	18.03	3.02(0.39)	2.06(0.09)	0.49(0.15)	2.70	4.81
$MnSe_2$	3.4912	$d_{z^2}+e_{1g}$	1.19	17.71	2.79(0.32)	1.88(0.06)	0.45(0.12)	2.35	5.63
$MnTe_2$	3.7448	$d_{z^2}+e_{1g}$	2.38	15.46	2.22(0.30)	1.45(0.07)	0.36(0.11)	0.93	5.92
FeS_2	3.2013	$d_{z^2}+e_{1g}$	1.51	18.34	3.13(0.60)	2.19(0.37)	0.46(0.11)	2.07	4.13
$FeSe_2$	3.3682	$d_{z^2}+e_{1g}$	1.69	17.98	2.81(0.56)	1.86(0.32)	0.46(0.12)	1.66	4.59
$FeTe_2$	3.6269	$d_{z^2}+e_{1g}$	2.55	12.80	1.63(0.44)	1.07(0.26)	0.29(0.08)	0.64	3.61
CoS_2	3.2281	$d_{z^2}+e_{1g}$	1.54	13.19	2.06(1.02)	1.58(0.50)	0.42(0.25)	1.34	2.20
$CoSe_2$	3.3704	$d_{z^2}+e_{1g}$	2.63	12.13	1.93(0.74)	1.50(0.40)	0.30(0.15)	0.73	1.31
$CoTe_2$	3.6227	$d_{z^2}+e_{1g}$	2.72	10.58	1.57(0.59)	1.06(0.32)	0.24(0.12)	0.58	0.98
NiS_2	3.3583	e_{2g}	1.75	18.23	3.05(2.30)	2.06(1.56)	0.48(0.38)	1.74	0.00
		d	3.58	21.46	3.67(2.62)	2.41(1.33)	0.63(0.54)	1.02	0.00
$NiSe_2$	3.5492	e_{2g}	1.86	18.01	2.16(1.80)	1.02(0.82)	0.58(0.48)	1.16	0.00
		d	3.49	20.28	3.09(2.39)	1.97(1.06)	0.61(0.50)	0.88	0.00
$NiTe_2$	3.7806	e_{2g}	2.13	17.65	1.88(1.42)	0.97(0.71)	0.45(0.35)	0.88	0.00
		d	4.32	18.45	2.65(1.87)	1.62(0.92)	0.53(0.41)	0.61	0.00

B. Effective Coulomb interactions

Now, we discuss the value of average on-site bare (unscreened) Coulomb interaction V, the average on-site partially (fully) screened interaction parameters U $(\tilde{U})$, as well as exchange interaction $J(\tilde{J})$ for correlated electrons of MX_2 systems. The results for $1T$-MX_2 and $2H$-MX_2 are presented in Tables I and II respectively. In both $2H$ and $1T$ structures, bare interaction V increases with increasing the number of electrons in the d-shell. This is to be expected because moving from the left Ti to the right Ni in the periodic table, the nuclear charge increases which leads to the contraction of d-wave functions, and subsequently increase the localization of the Wannier functions. Note that, the values of V reach a maximum for FeX_2 systems and drop off sharply for CoX_2. For a better understanding, we plot the shape of Wannier orbitals for $2H$-$CoSe_2$ systems in Fig. 4(c). The result indicates that the coupling of e_g states to neighboring chalcogen p states is significant, which leads to delocalization and, therefore, to smaller V interaction in Co case. Furthermore, the results for the chalcogen series MX_2 with X=S to Te shows a reduction in bare V, which is well understood by the increase in the lattice constant, making the Wannier function more extended.

The calculated U values for $1T$-MX_2 ($2H$-MX_2) lie between 1.4 and 3.7 eV (1.1 and 3.6 eV) and depend on the ground-state electronic structure, d-electron number, chalcogen X, and correlated subspace. Since all screening channels with an excitation energy larger than a few eV around E_F are contributed to in cRPA calculations of MX_2 systems, we see strong screening with large difference V-U values in these materials. As seen in Tables I and II, the U for M sites tend to increase when M is varied from Ti to Fe. In each chalcogen X and a particular subspace, the Hubbard U parameter is determined by two effects: (i) the Wannier localization effect due to increasing d-electron number and (ii) electronic structure effects. Similar to the bare interaction, the first effect is important also in Hubbard U which tends to enhance from Ti to Ni. For the second effect, the insight from orbital-resolved DOS of $1T$ structure ($2H$ structure) depicted in Fig. 5 (Fig. 6) is that below the d states there is a broad peak of chalcogen p orbitals, which should contribute with $p \rightarrow t'_{2g}$ ($p \rightarrow d_{z^2}+e_g$) transitions substantially to the screening. Indeed, as we move from Ti to Ni, the chalcogen p states gradually move to the lower energy and are accompanied by TM $3d$ bands. So, the contribution of the $p \rightarrow d$ transition into the polarization function does not change and even slightly reduces when moving from Ti to Fe and gives rise to the enhancement of U parameters with increasing $3d$ electron number in both $1T$ and $2H$ structures of TMDCs. Furthermore, there is another important screening processes via $t'_{2g} \rightarrow e_{2g}$ ($d_{z^2}+e_g \rightarrow e'_g$) in the $1T$ monolayer ($2H$ monolayer) of MX_2 systems, which only reduce the values of Coulomb parameters and does not change the trend across the TM series.

Schonhoff *et al.* [72] determined Hubbard U values for $2H$-VS_2 ($2H$-VSe_2) by employing the cRPA method. The obtained U values are 2.25 eV (2.40 eV), which are smaller than the calculated Coulomb interactions with $d_{z^2}+e_g$ subspace 3.12 eV (2.96 eV) and larger than the Coulomb interactions with d_{z^2} subspace 1.51 eV (1.43 eV) presented in Table II. Using the linear response approach, Isaacs *et al.* calculated

TABLE II. The same as Table I for $2H$ structure of MX_2.

MX_2	a(Å)	Orbitals	W_b (eV)	V (eV)	$U(\tilde{U})$ (eV)	$U'(\tilde{U}')$ (eV)	$J(\tilde{J})$ (eV)	U/W_b	$D(E_F)$
TiS_2	3.3376	$d_{z^2}+e_g$	2.23	14.47	2.88(2.62)	2.02(1.74)	0.52(0.41)	1.29	0.00
		d_{z^2}	1.20	13.92	1.83	–	–	1.53	0.00
$TiSe_2$	3.4739	$d_{z^2}+e_g$	2.39	14.18	2.55(2.26)	1.70(1.32)	0.51(0.39)	1.07	0.00
		d_{z^2}	1.05	13.26	1.62	–	–	1.54	0.00
$TiTe_2$	3.7277	$d_{z^2}+e_g$	2.78	13.43	2.03(1.59)	1.25(0.88)	0.47(0.36)	0.73	0.00
		d_{z^2}	0.96	13.09	1.27	–	–	1.32	0.00
VS_2	3.1650	$d_{z^2}+e_g$	2.97	15.05	3.12(1.16)	2.23(0.59)	0.55(0.34)	1.05	1.52
		d_{z^2}	0.95	14.49	1.51	–	–	1.59	0.65
VSe_2	3.3066	$d_{z^2}+e_g$	3.02	14.73	2.94(0.81)	2.01(0.33)	0.53(0.31)	0.97	1.80
		d_{z^2}	0.76	14.24	1.43	–	–	1.88	0.62
VTe_2	3.5458	$d_{z^2}+e_g$	3.40	14.05	2.45(0.65)	1.40(0.25)	0.49(0.29)	0.72	1.72
		d_{z^2}	0.69	13.40	1.12	–	–	1.62	0.51
CrS_2	3.0552	$d_{z^2}+e_g$	3.41	15.53	3.18(1.96)	2.28(1.43)	0.56(0.34)	0.93	0.00
$CrSe_2$	3.2108	$d_{z^2}+e_g$	3.62	15.31	2.93(1.67)	2.01(1.15)	0.53(0.33)	0.81	0.00
$CrTe_2$	3.4319	$d_{z^2}+e_g$	3.90	14.49	2.36(1.21)	1.55(0.88)	0.52(0.33)	0.61	0.00
MnS_2	3.0944	$d_{z^2}+e_g$	3.09	17.11	3.46(0.82)	2.42(0.50)	0.62(0.26)	1.12	1.78
$MnSe_2$	3.2335	$d_{z^2}+e_g$	3.32	16.92	3.10(0.68)	2.08(0.42)	0.61(0.24)	0.93	1.65
$MnTe_2$	3.5164	$d_{z^2}+e_g$	3.68	16.32	2.68(0.53)	1.79(0.32)	0.58(0.23)	0.73	2.05
FeS_2	3.1426	$d_{z^2}+e_g$	3.13	18.59	3.58(1.14)	2.45(0.67)	0.67(0.25)	1.14	1.75
$FeSe_2$	3.3040	$d_{z^2}+e_g$	3.18	18.46	3.31(1.06)	2.19(0.62)	0.67(0.24)	1.04	1.94
$FeTe_2$	3.5238	$d_{z^2}+e_g$	3.29	17.68	2.74(0.95)	1.76(0.54)	0.61(0.22)	0.83	1.81
CoS_2	3.2037	e_g	2.45	13.40	1.88(0.67)	1.40(0.44)	0.44(0.29)	0.77	2.07
$CoSe_2$	3.3406	e_g	2.51	12.93	1.72(0.61)	1.26(0.38)	0.43(0.28)	0.68	1.96
$CoTe_2$	3.5485	e_g	2.73	11.50	1.59(0.53)	1.11(0.36)	0.43(0.28)	0.58	2.18
NiS_2	3.4782	$e_g+e'_g$	2.96	16.99	3.07(0.99)	2.36(0.75)	0.45(0.32)	1.04	0.74
		e'_g	1.31	16.23	1.92(0.75)	1.24(0.62)	0.45(0.31)	1.47	0.42
$NiSe_2$	3.4263	$e_g+e'_g$	3.15	15.17	2.61(0.82)	1.94(0.63)	0.39(0.31)	0.83	0.67
		e'_g	1.43	14.38	1.66(0.57)	0.92(0.49)	0.37(0.27)	1.16	0.39
$NiTe_2$	3.6122	$e_g+e'_g$	3.23	13.22	1.91(0.62)	1.40(0.47)	0.36(0.27)	0.59	0.69
		e'_g	1.60	12.81	1.17(0.41)	0.55(0.28)	0.35(0.26)	0.73	0.37

U values for $2H$ structure of VS_2 in the nonmagnetic state and obtained $U = 4.14$ eV [10]. This value is almost 1.0-eV larger than the Hubbard interaction in Table II. For the magnetic state, they also determined U interactions for both $1T$ and $2H$ structures and obtained 3.84 eV for $2H$ structure and 3.99 eV for the $1T$ structure. What subspace to use in the construction of the Wannier basis or how to define as the Hubbard U parameter are the possible reasons for this disagreement.

Note that exclusive correlated subspaces must be incorporated into the U calculation, thus, it becomes imprecise to compare the Coulomb matrix elements results of $2H$-MX_2 (M=Ti,V,Co,Ni) and $1T$-NiX_2 monolayers with the corresponding results of other MX_2 compounds. For instance, considering the single band d_{z^2} as a correlated subspace for $2H$ structure of VSe_2, there is an extra sizable screening channel via the $d_{z^2} \rightarrow e_g$ transition, which can reduce Hubbard U with respect to U for the $d_{z^2}+e_g$ subspace. On the other hand, the value of $U = 1.43$ eV for $2H$-VSe_2 is smaller than the $U = 1.62$ eV for $2H$-$TiSe_2$, which does not follow the increasing trend across the TM series. It can be described by the M-$3d$ and X-p projected DOS around the E_F in Fig. 6. Indeed, as we go from Ti to V in the $2H$ structure of MX_2, the Se $-$ $4p$ states move towards d_{z^2} resulting in more contribution into the polarization function. It compensates for the increase in U caused by Wannier localization, leading to the reduction of U interaction with increasing $3d$ electron number. The same behavior is also observed in S- and Te-based $2H$-MX_2 materials (see Table II).

Ongoing from S to Te within each MX_2 system, the lattice constant increases, as a consequence, the longer bond lengths lead to smaller orbitals overlapping. It can bring the states closer together energetically as shown in Fig. 5 for the $1T$ structure, and thus a smaller energy difference increases the contribution of $p \rightarrow t'_{2g}$ and $t'_{2g} \rightarrow e_{2g}$ transitions ($p \rightarrow d_{z^2}+e_g$ and $d_{z^2}+e_g \rightarrow e'_g$ transition in $2H$-MX_2) into the polarization functions. This means that Coulomb screening is enhanced in the MS_2-MSe_2-MTe_2 sequence and thus the effective Coulomb interaction U reduces in the same sequence in both $1T$ and $2H$ structures. The situation for compounds with other correlated subspaces is almost the same. For instance, considering the d_{z^2} correlated subspace the U value is reduced in VTe_2 with respect to the VS_2 case.

In Table I, moving again from Ti to Ni, the same increasing trend is observed for partially interorbital Coulomb interactions U'. The obtained J parameters for MX_2 vary in the range 0.24–0.67 eV. Despite the very different range of values in respect to U and U', exchange J gradually increase with the d-electron number, which is less affected by the electronic structures. In cubic symmetry, Coulomb matrix elements, namely U and U', and J fulfills the relation $U' = U - 2J$. Even though TMDCs do not have cubic symmetry, this relation is nearly satisfied in most of them.

So far, we focused on the partially screened Coulomb interactions U. To analyze the screening within the correlated subspace, we also calculate fully screened Coulomb interactions $\tilde{U}$ and report within the parentheses for $1T$-MX_2 ($2H$-MX_2) in Table I (Table II). Except for the semiconductors $1T$-NiX_2, $2H$-TiX_2, and $2H$-CrX_2, the efficient metallic screening even causes more than 80% difference between U and $\tilde{U}$ parameters. Actually, the calculated $\tilde{U}$ parameters depend strongly on the DOS at the vicinity of E_F. For example, as seen in Table I, the $\tilde{U}$ value for VSe$_2$ in $1T$ structure ($2H$ structure) is 0.83 eV (0.81 eV) being about 60% smaller than $U = 2.14$ eV (2.94 eV) due to the large DOS at E_F and subsequently significant contribution of the $t'_{2g} \rightarrow t'_{2g}$ ($d_{z^2} + e_g \rightarrow d_{z^2} + e_g$) transitions to the polarization function. On the opposite side, in $2H$-TiX_2, $1T$-NiX_2, and $2H$-CrX_2, the screening within the correlated subspace is very weak due to the presence of the band gap in the electronic structures and $(U - \tilde{U})/U$ reaches 15–25% in these materials. Therefore, the behavior of fully screened interactions $\tilde{U}$ is completely different from U, as they do not follow the ordering with respect to increasing of d-electron number.

C. Strength of the electronic correlations and Stoner criterion

In the following, we discuss the strength of the electronic correlations, namely the ratio of the effective Coulomb interaction U to the bandwidth W_b (U/W_b) in $3d$-TMDCs. Note that the U/W_b values are determined for a non-spin-polarized state. Let us start with the results for $1T$ structures presented in Table I. For most of the $1T$-MX_2 compounds, we find $1 < U/W_b < 2$, which puts these systems in the moderately correlated regime. Therefore, Coulomb interaction plays an important role in the model Hamiltonian study of the correlation effects in the $1T$ single layer of TMDCs, which induce correlated phenomena like magnetic order. Starting from $1T$-TiX_2, the correlation strength U/W_b increases and reaches the maximum in Mn-based TMDC, and then tends to decrease to Co-based systems. Moreover, electron correlation is strong $U/W_b > 2$ in $1T$-MnX_2 (X=S, Se) materials, as a result, besides magnetic ordering, it can be unstable to the Mott phase.

The U/W_b for the $2H$ monolayer of $3d$-TMDCs does not show any clear trend with significant fluctuation around $U/W_b = 1$ from one system to another. We find that in $2H$-MX_2 (M = Ti, V) with d_{z^2} correlated subspace, the correlation strength U/W_b lie in the range between 1.3–1.9 eV. So, we expect rich correlated states such as magnetic order, Mott insulating phase, and so on in the $2H$-MX_2 with nearly half-filled bands. This provides good agreement with the DFT + U results [10,11] in which they indicate that the monolayer of H-VX_2 (X=S, Se) exhibits strong correlation effects, where the stability, phonon spectra, and magnetic moments are very sensitive to the effective Hubbard U and exchange J interactions. The Mott phase in layered materials containing TM atoms has been experimentally discovered in TM-halides such as CrI$_3$ [3,15] and VI$_3$ [22], other TMDCs such as $1T$-NbX_2 and $1T$-TaX_2 [43,44], and TM phosphorous trichalcogenides [45] like NiPX_3, where X=S and Se, which was confirmed by *ab initio* results [84,85]. There is one thing in common in all mentioned layered systems, and that is the presence of flat bands in the energy spectrum. For instance, a flat band with mainly d_{z^2} character at E_F increases U/W_b substantially in the distorted phase of $1T$-TaX_2 [86,87]. Here, there is also a half-filled isolated low-energy band with predominantly d_{z^2} character in $2H$-VX_2, resulting in an large U/W_b ratio, and is responsible for Mott insulating behavior.

It is interesting to compare our calculated U/W_b values with reported ones for elementary TMs and other layered materials containing TM atoms. While, the obtained $1 < U/W_b < 2$ values for TMDC compounds turn out to be larger than the corresponding $U/W_b < 1$ values in elementary transition metals [6], they are significantly smaller than the ones calculated $U/W_b > 2$ for TM-halides [7]. $U/W_b \sim 1$ were found in the case of M_2C and M_2CO$_2$ MX-enes, which reveals moderate electronic correlations in these materials [8]. Note that, although the *ab initio* Coulomb parameters of $3d$-TMDCs are smaller than elementary $3d$ TMs and MX-enes, the narrow bands with d_{z^2}, e_{1g}, and e_g character presented in TMDCs result in a larger U/W_b correlation strength.

As seen above, most of the metallic TMDC compounds having almost large correlation strength are expected to display correlation phenomena, such as ferromagnetic ordering. So, in the following, we discuss the appearance of ferromagnetism in these materials. Note that ignoring semiconductors $1T$-NiX_2, $2H$-TiX_2, and $2H$-CrX_2, the correlated subspace of all compounds are partially filled in the non-spin-polarized calculation, thus the Stoner model is well suited to explain the origin of the ferromagnetism of metallic $3d$-TMDCs. Based on this model, the instability of the paramagnetic state towards ferromagnetic ordering is given by the Stoner criterion $ID(E_F) > 1$, where I is the Stoner parameter and $D(E_F)$ is the DOS at the E_F in the nonmagnetic state. Solving the multiorbital Hubbard model, Stollhoff *et al.* found that the relationship between the Stoner parameter I, Hubbard U, and exchange J is given by $I = 3(U + 6J)/25$ [88]. On the basis of the calculated effective Coulomb parameters U and J presented in Tables I and II, $ID(E_F)$ values for all compounds are presented in Figs. 7(a) to 7(c). Among the metallic MX_2, only $2H$-NiX_2(X=S, Se, Te), $1T$-TiX_2 (X=S, Se, Te), CrS$_2$, and CoX_2(X=Se, Te) do not satisfy the Stoner criterion. Almost all theoretically predicted ferromagnetic $3d$-TMDCs fulfill the Stoner criterion, which is reasonably consistent with our results of spin-polarized total energy calculations and the sizable magnetic moments presented in right panels of Figs. 7(d) to 7(f). Almost the same value of $I.D(E_F)$ Stoner criterion calculated from d_{z^2} and $d_{z^2} + e_g$ subspaces is very noteworthy since the involved U and J parameters are rather different. Note that the simple Stoner model does not predict correctly the ground-state magnetic phase of $2H$-CoX_2 (X=S, Se, Te) and $1T$-CoS$_2$. Despite the value of $ID(E_F)$ for these materials being larger than 1, they have a nonmagnetic ground state.

$2H$-VSe$_2$ and $1T$-MnS$_2$ were among the first $3d$-TMDC materials in which room-temperature ferromagnetism was detected experimentally in the monolayer limit. Despite this, a few works indicated that the ferromagnetism observed in the $3d$-TMDCs is not intrinsic and stems from defects or proximity effects [52–54]. Also, controversy exists over the Mott insulating behavior in the monolayer of $3d$-TMDCs.

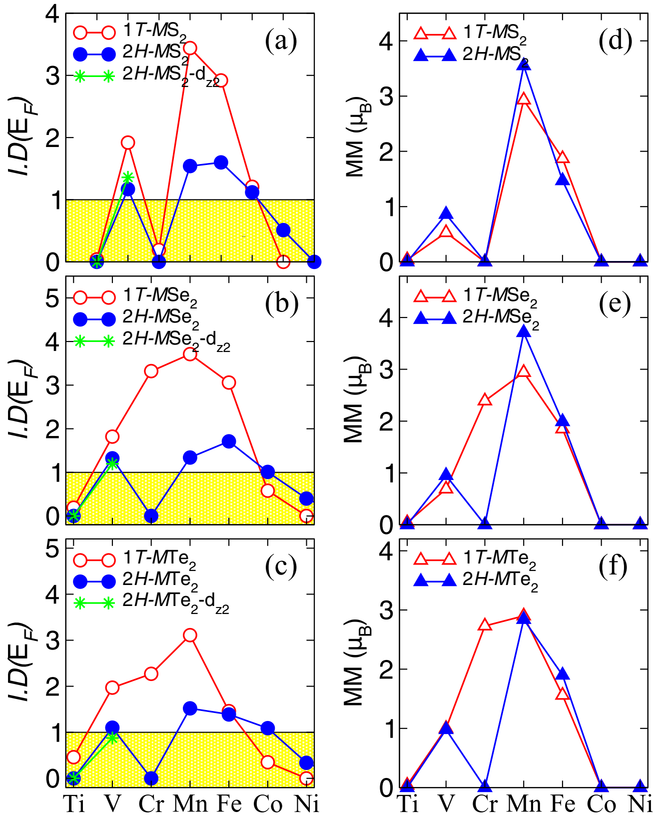

FIG. 7. Stoner criterion for both $1T$ and $2H$ structures of (a) $M\mathrm{S}_2$, (b) $M\mathrm{Se}_2$, and (c) $M\mathrm{Te}_2$. Calculated magnetic moments (in units of μ_B) of TM atoms for (d) $M\mathrm{S}_2$, (e) $M\mathrm{Se}_2$, and (f) $M\mathrm{Te}_2$. We also presented the values in the case of d_{z^2} correlated subspace with green star points in $2H$ structures.

From the theoretical side, the electronic and magnetic ground state depends strongly on taking the correct Hubbard U parameter of the d electrons into account in model Hamiltonian or first-principle calculation. As shown in Fig. 7, in the case of $1T$-MnS$_2$, the criterion $ID(E_F) > 1$ is easily satisfied that explains why a relatively strong ferromagnetic order is observed in the experiment. Also, its correlation strength $U/W_b = 2.7$ reinforces this idea that the preferred magnetic order is ferromagnetic. The situation in the case of $2H$ structure of VSe$_2$ is not straightforward. We find $ID(E_F) \sim 1$ which puts system close to the edge of paramagnetic to ferromagnetic transition (see left panels of Fig. 7). It may explain why there is no agreement in the magnetic phase of VX_2 materials.

IV. CONCLUSION

We systematically determined the correlated subspaces and effective on-site and interorbital Coulomb interactions between localized electrons in $3d$ MX_2 (M=Ti, V, Cr, Mn, Fe, Co, Ni, and X=S, Se and Te) by employing first *ab initio* calculations in conjunction with a parameter-free cRPA scheme. These Coulomb interactions not only provide a fundamental understanding of the correlated phenomena such as magnetic ordering, charge density wave, or Mott phase in $3d$-TMDCs, but these effective cRPA parameters can also be used in model Hamiltonians thus increasing the predictive power of model calculations. Based on the Hubbard U, exchange interactions J, and electronic structure, we find that, for most of the TMDC compounds, the correlation strength U/W_b are large enough to be able to put them in moderate and even strong correlated regimes. Among TMDC materials, the maximum value $U/W_b = 2.7\,\mathrm{eV}$ is obtained in MnS$_2$ which is almost three times larger than the corresponding value in elementary Mn. We thus expect electron correlations to play an important role in model Hamiltonian studies of the $3d$-TMDCs. Since, there is no agreement on the magnetic ordering of these materials, in particular, experimentally observed systems like VSe$_2$ and MnS$_2$, we checked the condition to be fulfilled for the formation of ferromagnetic order by Stoner criterion $ID(E_F) > 1$. The results indicate that both MnX_2 (X=S, Se) and VX_2 (X=S, Se) have an intrinsic ferromagnetic behavior in pristine form, with a difference that V-based materials are in close vicinity to the critical point separating the ferromagnetic from the paramagnetic phase.

ACKNOWLEDGMENTS

The authors acknowledge the computational resources provided by the Physics Department of the University of Guilan.

---

[1] A. K. Geim and K. S. Novoselov, Nat. Mater. **6**, 183 (2007).

[2] M. I. Katsnelson, Mater. Today **10**, 20 (2007).

[3] B. Huang, G. Clark, E. Navarro-Moratalla, D. R. Klein, R. Cheng, K. L. Seyler, D. Zhong, E. Schmidgall, M. A. McGuire, D. H. Cobden, W. Yao, Di Xiao, P. Jarillo-Herrero, and X. Xu, Nature (London) **546**, 270 (2017).

[4] Ch. Gong, L. Li, Zh. Li, H. Ji, A. Stern, Y. Xia, T. Cao, W. Z. Q. Qiu, R. J. Cava, S. G. Louie, J. Xia, and X. Zhang, Nature (London) **546**, 265 (2017).

[5] W. Yu, J. Li, T. S. Herng, Z. Wang, X. Zhao, X. Chi, W. Fu, I. Abdelwahab, J. Zhou, J. Dan, Z. Chen, Z. Chen, Z. Li, J. Lu, S. J. Pennycook, Y. P. Feng, J. Ding, and K. P. Loh, Adv. Mater. **31**, 1903779 (2019).

[6] E. Sasioglu, C. Friedrich, and S. Blugel, Phys. Rev. B **83**, 121101(R) (2011); Phys. Rev. Lett. **109**, 146401 (2012).

[7] Y. Yekta, H. Hadipour, E. Sasioglu, C. Friedrich, S. A. Jafari, S. Blugel, and I. Mertig, Phys. Rev. Materials **5**, 034001 (2021).

[8] H. Hadipour and Y. Yekta, Phys. Rev. B **100**, 195118 (2019).

[9] Y. D. Wang, W. L. Yao, Z. M. Xin, T. T. Han, Z. G. Wang, L. Chen, C. Cai, Y. Li, and Y. Zhang, Nat. Commun. **11**, 4215 (2020).

[10] Eric B. Isaacs and Chris A. Marianetti, Phys. Rev. B **94**, 035120 (2016).

[11] H. L. Zhuang and R. G. Hennig, Phys. Rev. B **93**, 054429 (2016)

[12] M. A. McGuire, G. Clark, S. KC, W. M. Chance, G. E. Jellison, Jr., V. R. Cooper, X. Xu, and B. C. Sales, Phys. Rev. Materials **1**, 014001 (2017).

[13] Zh. Zhang, J. Shang, Ch. Jiang, A. Rasmita, W. Gao, and T. Yu, Nano Lett. **19**, 3138 (2019).

[14] M. C. De Siena, S. E. Creutz, A. Regan, P. Malinowski, Q. Jiang, K. T. Kluherz, Gu. Zhu, Zh. Lin, J. J. De Yoreo, X. Xu, J. H. Chu, and D. R. Gamelin, Nano Lett. **20**, 2100 (2020).

[15] K. L. Seyler, D. Zhong, D. R. Klein, Sh. Gao, X. Zhang, B. Huang, E. Navarro-Moratalla, L. Yang, D. H. Cobden, M. A. McGuire, W. Yao, D. Xiao, P. Jarillo-Herrero, and X. Xu, Nat. Phys. **14**, 277 (2018).

[16] D. Shcherbakov, P. Stepanov, D. Weber, Y. Wang, J. Hu, Y. Zhu, K. Watanabe, T. Taniguchi, Zh. Mao, W. Windl, J. Goldberger, M. Bockrath, and Ch. N. Lau, Nano Lett. **18**, 4214 (2018).

[17] Sh. Jiang, L. Li, Z. Wang, K. F. Mak, and J. Shan, Nat. Nanotechnol. **13**, 549 (2018).

[18] S. Son, M. J. Coak, N. Lee, J. Kim, T. Y. Kim, H. Hamidov, H. Cho, Ch. Liu, D. M. Jarvis, Ph. A. C. Brown, J. H. Kim, Ch. H. Park, D. I. Khomskii, S. S. Saxena, and J. G. Park, Phys. Rev. B **99**, 041402(R) (2019).

[19] T. Kong, K. Stolze, E. I. Timmons, J. Tao, D. Ni, S. Guo, Z. Yang, R. Prozorov, and R. J. Cava, Adv. Mater. **31**, 1808074 (2019).

[20] T. Kurumaji, S. Seki, S. Ishiwata, H. Murakawa, Y. Kaneko, and Y. Tokura, Phys. Rev. B **87**, 014429 (2013).

[21] O. Besbes, S. Nikolaev, N. Meskini, and I. Solovyev, Phys. Rev. B **99**, 104432 (2019).

[22] Sh. Tian, J. F. Zhang, Ch. Li, T. Ying, Sh. Li, X. Zhang, K. Liu, and H. Lei, J. Am. Chem. Soc. **141**, 5326 (2019).

[23] J. He, Sh. Ma, P. Lyua, and P. Nachtigall, J. Mater. Chem. C **4**, 2518 (2016).

[24] J. Liu, Q. Sun, Y. Kawazoed, and P. Jenac, Phys. Chem. Chem. Phys. **18**, 8777 (2016).

[25] D. Torelli, K. S. Thygesen, and T. Olsen, 2D Mater. **6**, 045018 (2019).

[26] Y. Deng, Y. Yu, Y. Song, J. Zhang, N. Z. Wang, Z. Sun, Y. Yi, Y. Z. Wu, S. Wu, J. Zhu, J. Wang, X. H. Chen, and Y. Zhang, Nature (London) **563**, 94 (2018).

[27] Z. Fei, B. Huang, P. Malinowski, W. Wang, T. Song, J. Sanchez, W. Yao, D. Xiao, X. Zhu, A. F. May, W. Wu, D. H. Cobden, J.-H. Chu, and X. Xu, Nat. Mater. **17**, 778 (2018).

[28] J. Li, B. Zhao, P. Chen, R. Wu, B. Li, Q. Xia, G. Guo, J. Luo, K. Zang, Z. Zhang, H. Ma, G. Sun, X. Duan, and X. Duan, Adv. Mater. **30**, 1801043 (2018).

[29] G. Duvjir, B. K. Choi, I. Jang, S. Ulstrup, S. Kang, T. T. Ly, S. Kim, Y. H. Choi, C. Jozwiak, A. Bostwick, E. Rotenberg, J.-G. Park, R. Sankar, K.-S. Kim, J. Kim, and Y. J. Chang, Nano Lett. **18**, 5432 (2018).

[30] M. Bonilla, S. Kolekar, Y. Ma, H. C. Diaz, V. Kalappattil, R. Das, T. Eggers, H. R. Gutierrez, M. H. Phan, and M. Batzill, Nat. Nanotechnol. **13**, 289 (2018).

[31] Y. Guo, H. Deng, X. Sun, X. Li, J. Zhao, J. Wu, W. Chu, S. Zhang, H. Pan, X. Zheng, X. Wu, C. Jin, C. Wu, and Y. Xie, Adv. Mater. **29**, 1700715 (2017).

[32] Y. Ma, Y. Dai, M. Guo, C. Niu, Y. Zhu, and B. Huang, ACS Nano **6**, 1695 (2012).

[33] X. Wang, D. Li, Z. Li, C. Wu, C.-M. Che, G. Chen, and X. Cui, ACS Nano **15**, 16236 (2021).

[34] K. Lasek, P. M. Coelho, K. Zberecki, Y. Xin, S. K. Kolekar, J. Li, and M. Batzill, ACS Nano **14**, 8473 (2020).

[35] D. J. OHara, T. Zhu, A. H. Trout, A. S. Ahmed, Y. K. Luo, Ch. H. Lee, M. R. Brenner, S. Rajan, J. A. Gupta, D. W. McComb, and R. K. Kawakami, Nano Lett. **18**, 3125 (2018).

[36] H. L. Zhuang, M. D. Johannes, M. N. Blonsky, and R. G. Hennig, Appl. Phys. Lett. **104**, 022116 (2014).

[37] D. C. Freitas, R. Weht, A. Sulpice, G. Remenyi, P. Strobel, F. Gay, J. Marcus, and M. Nsunez-Regueiro, J. Phys.: Condens. Matter **27**, 176002 (2015).

[38] X. Sun, W. Li, X. Wang, Q. Sui, T. Zhang, Z. Wang, L. Liu, D. Li, S. Feng, S. Zhong, H. Wang, V. Bouchiat, M. Nunez Regueiro, N. Rougemaille, J. Coraux, A. Purbawati, A. Hadj-Azzem, Z. Wang, B. Dong, X. Wu, T. Yang, G. Yu, B. Wang, Z. Han, X. Han, and Z. Zhang, Nano Res. **13**, 3358 (2020).

[39] A. Purbawati, J. Coraux, J. Vogel, A. Hadj-Azzem, N. Wu, N. Bendiab, D. Jegouso, J. Renard, L. Marty, V. Bouchiat, A. Sulpice, L. Aballe, M. Foerster, F. Genuzio, A. Locatelli, T. O. Mentes, Z. V. Han, X. Sun, M. Nunez-Regueiro, and N. Rougemaille, ACS Appl. Mater. Interfaces **12**, 30702 (2020).

[40] Md. R. Habib, S. Wang, W. Wang, H. Xiao, S. K. Md. Obaidulla, A. Gayen, Y. Khan, H. Chen, and M. Xu, Nanoscale **11**, 20123 (2019).

[41] B. Li, Z. Wan, C. Wang, P. Chen, B. Huang, X. Cheng, Q. Qian, J. Li, Z. Zhang, G. Sun, B. Zhao, H. Ma, R. Wu, Z. Wei, Y. Liu, L. Liao, Y. Ye, Y. Huang, X. Xu, X. Duan, W. Ji, and X. Duan, Nat. Mater. **20**, 818 (2021).

[42] L. Meng, Z. Zhou, M. Xu, S. Yang, K. Si, L. Liu, X. Wang, H. Jiang, B. Li, P. Qin, P. Zhang, J. Wang, Z. Liu, P. Tang, Y. Ye, W. Zhou, L. Bao, H.-J. Gao, and Y. Gong, Nat. Commun. **12**, 809 (2021).

[43] L. Perfetti, A. Georges, S. Florens, S. Biermann, S. Mitrovic, H. Berger, Y. Tomm, H. Hochst, and M. Grioni, Phys. Rev. Lett. **90**, 166401 (2003).

[44] T. Ritschel, J. Trinckauf, K. Koepernik, B. Büchner, M. V. Zimmermann, H. Berger, Y. I. Joe, P. Abbamonte, and J. Geck, Nat. Phys. **11**, 328 (2015).

[45] S. Y. Kim, T. Y. Kim, L. J. Sandilands, S. Sinn, M.-C. Lee, J. Son, S. Lee, K.-Y. Choi, W. Kim, B.-G. Park, C. Jeon, H.-D. Kim, C.-H. Park, J.-G. Park, S. J. Moon, and T. W. Noh, Phys. Rev. Lett. **120**, 136402 (2018).

[46] P. Chen, Y.-H. Chan, X.-Y. Fang, Y. Zhang, M. Y. Chou, S.-K. Mo, Z. Hussain, A.-V. Fedorov, and T.-C. Chiang, Nat. Commun. **6**, 8943 (2015).

[47] K. Sugawara, Y. Nakata, R. Shimizu, P. Han, T. Hitosugi, T. Sato, and T. Takahashi, ACS Nano **10**, 1341 (2016).

[48] J. Feng, D. Biswas, A. Rajan, M. D. Watson, F. Mazzola, O. J. Clark, K. Underwood, I. Markovi, M. McLaren, A. Hunter, D. M. Burn, L. B. Duffy, S. Barua, G. Balakrishnan, F. Bertran, P. Le Fèvre, T. K. Kim, G. van der Laan, T. Hesjedal, P. Wahl, and P. D. C. King, Nano Lett. **18**, 4493 (2018).

[49] P. Chen, W. W. Pai, Y.-H. Chan, V. Madhavan, M. Y. Chou, S.-K. Mo, A.-V. Fedorov, and T.-C. Chiang, Phys. Rev. Lett. **121**, 196402 (2018).

[50] A. O. Fumega, M. Gobbi, P. Dreher, W. Wan, C. Gonzalez-Orellana, M. Pena-Diaz, C. Rogero, J. Herrero-Martin, P. Gargiani, M. Ilyn, M. M. Ugeda, V. Pardo, and S. Blanco-Canosa, J. Phys. Chem. C **123**, 27802 (2019).

[51] P. K. J. Wong, W. Zhang, F. Bussolotti, X. Yin, T. S. Herng, L. Zhang, Y. L. Huang, G. Vinai, S. Krishnamurthi, D. W. J. A. M. Bukhvalov, Y. J. Zheng, R. Chua, A. T. N'Diaye, S. A. Morton, C.-Y. Yang, K.-H. Ou Yang, P. Torelli, W. Chen, K. Eng Johnson Goh, J. Ding, M.-T. Lin, G. Brocks, M. P. de Jong, A. H.

Castro Neto, and A. Thye Shen Wee, Adv. Mater. **31**, 1901185 (2019).

[52] G. Vinai, C. Bigi, A. Rajan, M. D. Watson, T.-L. Lee, F. Mazzola, S. Modesti, S. Barua, M. Ciomaga Hatnean, G. Balakrishnan, P. D. C. King, P. Torelli, G. Rossi, and G. Panaccione, Phys. Rev. B **101**, 035404 (2020).

[53] R. Chua, J. Yang, X. He, X. Yu, W. Yu, F. Bussolotti, P. K. J. Wong, K. P. Loh, M. B. H. Breese, K. E. Johnson Goh, Y. L. Huang, and A. T. S. Wee, Adv. Mater. **32**, 2000693 (2020).

[54] W. Zhang, L. Zhang, P. K. J. Wong, J. Yuan, G. Vinai, P. Torelli, G. van der Laan, Y. P. Feng, and A. T. S. Wee, ACS Nano **13**, 8997 (2019).

[55] O. V. Yazyev and L. Helm, Phys. Rev. B **75**, 125408 (2007).

[56] H. Hadipour, Phys. Rev. B **99**, 075102 (2019).

[57] E. Sasioglu, H. Hadipour, C. Friedrich, S. Blugel, and I. Mertig, Phys. Rev. B **95**, 060408(R) (2017).

[58] M. M. Ugeda, I. Brihuega, F. Guinea, and J. M. Gomez-Rodriguez, Phys. Rev. Lett. **104**, 096804 (2010).

[59] Z. Zhang, X. Zou, V. H. Crespi, and B. I. Yakobson, ACS Nano **7**, 10475 (2013).

[60] L. Cai, J. He, Q. Liu, T. Yao, L. Chen, W. Yan, F. Hu, Y. Jiang, Y. Zhao, T. Hu, Z. Sun, and S. Wei, J. Am. Chem. Soc. **137**, 2622 (2015).

[61] W.-Y. Tong, S.-J. Gong, X. Wan, and C.-G. Duan, Nat. Commun. **7**, 13612 (2016).

[62] L. Chengan, M. Yandong, Zh. Ting, X. Xilong, H. Baibiao, and D. Ying, New J. Phys. **22**, 033002 (2020).

[63] H.-R. Fuh, C.-R. Chang, Y.-K. Wang, R. F. L. Evans, R. W. Chantrell, and H.-T. Jeng, Sci. Rep. **6**, 32625 (2016).

[64] K. S. Thygesen, 2D Mater. **4**, 022004 (2017).

[65] F. A. Rasmussen and K. S. Thygesen, J. Phys. Chem. C **119**, 13169 (2015)

[66] M. Cazzaniga, H. Cercellier, M. Holzmann, C. Monney, P. Aebi, G. Onida, and V. Olevano, Phys. Rev. B **85**, 195111 (2012).

[67] M. Esters, R. G. Hennig, and D. C. Johnson, Phys. Rev. B **96**, 235147 (2017).

[68] C. Wang, X. Zhou, Y. Pan, J. Qiao, X. Kong, C.-C. Kaun, and W. Ji, Phys. Rev. B **97**, 245409 (2018).

[69] M. Cococcioni and S. de Gironcoli, Phys. Rev. B **71**, 035105 (2005).

[70] F. Aryasetiawan, M. Imada, A. Georges, G. Kotliar, S. Biermann, and A. I. Lichtenstein, Phys. Rev. B **70**, 195104 (2004); F. Aryasetiawan, K. Karlsson, O. Jepsen, and U. Schonberger, *ibid.* **74**, 125106 (2006); T. Miyake, F. Aryasetiawan, and M. Imada, *ibid.* **80**, 155134 (2009).

[71] Y. Nomura, M. Kaltak, K. Nakamura, C. Taranto, S. Sakai, A. Toschi, R. Arita, K. Held, G. Kresse, and M. Imada, Phys. Rev. B **86**, 085117 (2012); B.-C. Shih, Y. Zhang, W. Zhang, and P. Zhang, *ibid.* **85**, 045132 (2012).

[72] G. Schoenhoff, M. Rosner, E. Kamil, J. Berges, and T. Wehling, APS March Meeting Abstracts 2018, S35 (2018).

[73] Li. Fengyu, Tu. Kaixiong, and Z. Chen, J. Phys. Chem. C **118**, 21264 (2014).

[74] M. Rassekh, J. He, S. F. Shayesteh, and J. J. Palacios, Comput. Mater. Sci. **183**, 109820 (2020).

[75] X. Ou and H. Wu, Sci. Rep. **4**, 4609 (2015).

[76] F. Freimuth, Y. Mokrousov, D. Wortmann, S. Heinze, and S. Blugel, Phys. Rev. B **78**, 035120 (2008).

[77] http://www.flapw.de/.

[78] J. P. Perdew, K. Burke, and M. Ernzerhof, Phys. Rev. Lett. **77**, 3865 (1996).

[79] G. Pizzi, V. Vitale, R. Arita, S. Blügel, F. Freimuth, G. Géranton, M. Gibertini, D. Gresch, C. Johnson, T. Koretsune, J. Ibañez-Azpiroz, H. Lee, J.-M. Lihm, D. Marchand, A. Marrazzo, Y. Mokrousov, J. I Mustafa, Y. Nohara, Y. Nomura, L. Paulatto, S. Poncé, T. Ponweiser, J. Qiao, F. Thöle, S. S. Tsirkin, M. Wierzbowska, N. Marzari, D. Vanderbilt, I. Souza, A. A Mostofi, and J. R Yates, J. Phys.: Condens. Matter **32**, 165902 (2020).

[80] A. Schindlmayr, C. Friedrich, E. Sasioglu, and S. Blugel, Z. Phys. Chem. **224**, 357 (2010).

[81] C. Friedrich, S. Blugel, and A. Schindlmayr, Phys. Rev. B **81**, 125102 (2010).

[82] V. I. Anisimov, I. V. Solovyev, M. A. Korotin, M. T. Czyzyk, and G. A. Sawatzky, Phys. Rev. B **48**, 16929 (1993).

[83] V. Anisimov and Y. Izyumov, *Electronic Structure of Strongly Correlated Materials* (Springer, Berlin, 2010).

[84] H.-S. Kim, K. Haule, and D. Vanderbilt, Phys. Rev. Lett. **123**, 236401 (2019).

[85] S. H. Lee, J. S. Goh, and D. Cho, Phys. Rev. Lett. **122**, 106404 (2019).

[86] C. Tresca and M. Calandra, 2D Mater. **6**, 035041 (2019).

[87] E. Kamil, J. Berges, G. Schonhoff, M. Rosner, M. Schuler, G. Sangiovanni, and T. O. Wehling, J. Phys.: Condens. Matter **30**, 325601 (2018).

[88] G. Stollhoff, A. M. Oles, and V. Heine, Phys. Rev. B **41**, 7028 (1990).